ALMA confirmation of an obscured hyperluminous radio-loud AGN at $z = 6.853$ associated with a dusty starburst in the 1.5 deg^2 COSMOS field

Ryan Endsley [1,2][★] Daniel P. Stark,[1] Jianwei Lyu,[1] Feige Wang,[1] Jinyi Yang,[1]† Xiaohui Fan,[1]
Renske Smit,[3] Rychard Bouwens,[4] Kevin Hainline[1] and Sander Schouws[4]

[1]*Steward Observatory, University of Arizona, 933 N Cherry Avenue, Tucson, AZ 85721, USA*
[2]*Department of Astronomy, University of Texas, Austin, TX 78712, USA*
[3]*Astrophysics Research Institute, Liverpool John Moores University, 146 Brownlow Hill, Liverpool L3 5RF, UK*
[4]*Leiden Observatory, Leiden University, NL-2300 RA Leiden, the Netherlands*

ABSTRACT

We present band 6 ALMA observations of a heavily obscured radio-loud ($L_{1.4\,GHz} = 10^{25.4}$ W Hz^{-1}) active galactic nucleus (AGN) candidate at $z_{phot} = 6.83 \pm 0.06$ found in the 1.5 deg^2 COSMOS field. The ALMA data reveal detections of exceptionally strong [C II]158 μm ($z_{[C II]} = 6.8532$) and underlying dust continuum emission from this object (COS-87259), where the [C II] line luminosity, line width, and 158 μm continuum luminosity are comparable to those seen from $z \sim 7$ sub-mm galaxies and quasar hosts. The 158 μm continuum detection suggests a total infrared luminosity of 9×10^{12} L$_\odot$ with corresponding very large obscured star formation rate (1300 M$_\odot$ yr^{-1}) and dust mass (2×10^9 M$_\odot$). The strong break seen between the VIRCam and IRAC photometry perhaps suggests that COS-87259 is an extremely massive reionization-era galaxy with $M_* \approx 1.7 \times 10^{11}$ M$_\odot$. Moreover, the MIPS, PACS, and SPIRE detections imply that this object harbours an AGN that is heavily obscured ($\tau_{9.7\,\mu m} = 2.3$) with a bolometric luminosity of approximately 5×10^{13} L$_\odot$. Such a very high AGN luminosity suggests that this object is powered by an $\approx 1.6 \times 10^9$ M$_\odot$ black hole if accreting near the Eddington limit, and is effectively a highly obscured version of an extremely ultraviolet (UV)-luminous ($M_{1450} \approx -27.3$) $z \sim 7$ quasar. Notably, these $z \sim 7$ quasars are an exceedingly rare population (~ 0.001 deg^{-2}), while COS-87259 was identified over a relatively small field. Future very wide area surveys with e.g. *Roman* and *Euclid* have the potential to identify many more extremely red yet UV-bright $z \gtrsim 7$ objects similar to COS-87259, providing richer insight into the occurrence of intense obscured star formation and supermassive black hole growth among this population.

Key words: galaxies: high-redshift – quasars: supermassive black holes – submillimetre: galaxies – dark ages, reionization, first stars – galaxies: evolution.

1 INTRODUCTION

For much of the past two decades, deep imaging surveys with the *Hubble Space Telescope* (*HST*) have served as key windows on galaxies present in the first billion years of cosmic history (e.g. Giavalisco et al. 2004; Bouwens et al. 2011; Grogin et al. 2011; Koekemoer et al. 2011; Trenti et al. 2011; Ellis et al. 2013; Illingworth et al. 2013; Lotz et al. 2017). To date, these *HST* surveys have enabled the identification of over 1000 Lyman-break galaxies at $z \gtrsim 6$ (e.g. McLure et al. 2013; Finkelstein et al. 2015; Ishigaki et al. 2018; Oesch et al. 2018; Bouwens et al. 2021), the bulk of which are faint ($M_{UV} > -20$) star-forming systems thought largely responsible for cosmic reionization (Bouwens et al. 2015; Finkelstein et al. 2019; Robertson 2022). Overlapping deep rest-optical imaging with the *Spitzer* Infrared Array Camera (IRAC) has shown that these galaxies tend to possess low stellar masses ($M_* < 10^9$ M$_\odot$) and strong rest-

optical nebular line emission consistent with young ages (e.g. Labbé et al. 2013; Stark et al. 2013; Smit et al. 2014, 2015; Song et al. 2016; De Barros et al. 2019; Endsley et al. 2021a; Stefanon et al. 2021). However, while these *HST* surveys can push to extremely deep depths ($J \sim 29$), they tend to cover relatively small areas ($\lesssim 0.01$ deg^2) that do not statistically sample $z \gtrsim 6$ galaxies that are sufficiently bright for detailed characterization with existing facilities ($J \lesssim 25$). Consequently, our understanding of very early galaxies has long been primarily limited to their rest-ultraviolet (UV) + optical photometric properties.

Within the past few years, several deep wide-area ($>$deg^2) optical + near-infrared (IR) imaging surveys have reached (near) completion (Lawrence et al. 2007; McCracken et al. 2012; Jarvis et al. 2013; Inoue et al. 2020; Aihara et al. 2022), providing large samples of UV-bright ($-23 \lesssim M_{UV} \lesssim -21$) Lyman-break $z \gtrsim 7$ galaxies (Bowler et al. 2017, 2020; Stefanon et al. 2019; Endsley et al. 2021a; Bouwens et al. 2022; Harikane et al. 2022; Schouws et al. 2022a). This has in turn led to substantial improvements in our understanding of the UV-luminous reionization-era galaxy population. Rest-UV spectroscopic follow-up has revealed significant Lyman-alpha

---

★ E-mail: ryan.endsley@austin.utexas.edu
† Strittmatter Fellow.

emission from several of these systems (Ono et al. 2012; Furusawa et al. 2016; Endsley et al. 2021b, 2022b; Valentino et al. 2022), while (in some cases) simultaneously uncovering strong large-scale over-densities likely tracing very large ionized bubbles (Endsley & Stark 2022). Follow-up with the Atacama Large Millimeter/submillimeter Array (ALMA) has also been highly successful in detecting far-IR cooling lines ([C II]158 μm and [O III]88 μm) from several UV-bright $z \gtrsim 7$ galaxies (Smit et al. 2018; Hashimoto et al. 2019; Bouwens et al. 2022; Bowler et al. 2022; Schouws et al. 2022a), with a substantial fraction additionally exhibiting strong far-IR continuum emission indicating substantial obscured star formation activity (Hashimoto et al. 2019; Inami et al. 2022; Schouws et al. 2022b).

Alongside efforts to study Lyman-break $z \gtrsim 7$ galaxies, there has also been a dedicated push to identify and subsequently characterize UV-luminous quasars as well as IR-luminous sub-millimetre galaxies in this epoch. The 2500 deg^2 South Pole Telescope Survey (Everett et al. 2020) has resulted in the discovery of a sub-mm system at $z = 6.900$ (SPT-0311; Strandet et al. 2017), the only such source currently known at $z > 6.5$. ALMA follow-up revealed that this object is actually a merger of two galaxies exhibiting intense dust-obscured star formation activity (≈ 3500 M$_\odot$ yr^{-1} combined) that likely traces one of the most massive haloes in the reionization era ($\sim 3 \times 10^{12}$ M$_\odot$; Marrone et al. 2018; Spilker et al. 2022). Thanks to a rich collection of $\gtrsim 1000$ deg^2 optical + near-IR surveys, there are now more than 40 known extremely UV-luminous ($-28 \leq M_{UV} \leq -25$) quasars at $z > 6.5$ (Mortlock et al. 2011; Venemans et al. 2013, 2015; Mazzucchelli et al. 2017; Reed et al. 2017, 2019; Wang et al. 2017, 2018, 2019, 2021; Bañados et al. 2018, 2021; Matsuoka et al. 2018, 2019, 2022; Yang et al. 2019a, 2020b, 2021). These unobscured active galactic nuclei (AGNs) are powered by the earliest known supermassive black holes with masses of $M_{BH} \approx (0.3–3) \times 10^9$ M$_\odot$ accreting near the Eddington limit (e.g. Yang et al. 2021). Far-IR follow-up of these quasars has provided a window into their host galaxies, revealing that several of these systems show very bright [C II], CO, and dust continuum emission similar to sub-mm galaxies (e.g. Venemans et al. 2016, 2017a, b, 2020; Decarli et al. 2018, 2022; Yang et al. 2019b; Pensabene et al. 2021). One population that would help bridge the gap between known quasars and sub-mm galaxies at $z \gtrsim 7$ is heavily obscured AGNs. However, even though these obscured AGNs are expected to be more abundant than their unobscured counterparts (i.e. quasars) in the early Universe (Vito et al. 2018; Davies, Hennawi & Eilers 2019; Trebitsch, Volonteri & Dubois 2019; Ni et al. 2020; Lupi et al. 2022), to date no such object has been confirmed at $z > 6.5$.

We previously reported the photometric identification of a heavily obscured, hyperluminous AGN candidate at $z \simeq 6.83$ located in the 1.5 deg^2 Cosmic Evolution Survey (COSMOS) field (Endsley et al. 2022a, hereafter E22a). This source, COS-87259, was originally identified as a Lyman-break $z \simeq 6.6$–6.9 galaxy using deep optical + near-IR imaging (Endsley et al. 2021a), and was later found to exhibit a sharp spectral discontinuity between two intermediate/narrow bands at 9450 and 9700 Å suggesting $z_{phot} = 6.83 \pm 0.06$ (E22a). While similar in UV luminosity to many other wide-area-selected Lyman-break $z \sim 7$ galaxies ($J = 25.0$ AB; $M_{UV} = -21.7$), COS-87259 was found to show both an exceptionally red rest-UV slope ($\beta = -0.6$) and a prominent Balmer break in the *Spitzer*/IRAC bands, implying unusually strong dust attenuation as well as a relatively old, massive stellar population (Endsley et al. 2021a). Subsequent investigations revealed that this galaxy is also detected in the Multi-Band Imaging Photometer for *Spitzer* (MIPS), *Herschel* Photodetector Array Camera and Spectrometer (PACS), *Herschel* Spectral

and Photometric Imaging Receiver (SPIRE), James Clerk Maxwell Telescope (JCMT) Submillimetre Common-User Bolometer Array 2 (SCUBA-2), Very Large Array (VLA), Low Frequency Array (LOFAR), and MeerKAT bands (E22a). These data imply that, if at $z \simeq 6.8$, COS-87259 is undergoing rapid, highly obscured star formation activity and harbours a heavily obscured hyperluminous radio-loud ($L_{1.4\,GHz} = 10^{25.4}$ W Hz^{-1}) AGN (E22a).

Here, we report the ALMA spectroscopic confirmation of COS-87259 as well as detections of exceptionally strong [C II]158 μm and underlying dust continuum emission from this system. We describe the ALMA observations in Section 2 and then report the [C II] and dust continuum properties of COS-87259 in Section 3 comparing to other known objects at $z > 6.5$. We then discuss the physical properties of COS-87259 in Section 4. Our conclusions are summarized in Section 5, followed by a brief outlook on the potential of future *Roman* and *Euclid* surveys to identify many more extremely red, UV-bright $z \gtrsim 7$ galaxies similar to COS-87259. Throughout this paper, we quote magnitudes in the AB system (Oke & Gunn 1983), adopt a flat Lambda cold dark matter cosmology with parameters $h = 0.7$, $\Omega_M = 0.3$, and $\Omega_\Lambda = 0.7$, and report 68 per cent confidence interval uncertainties unless otherwise specified.

2 OBSERVATIONS

ALMA observations were conducted targeting the [C II]158 μm emission line from COS-87259 on 2022 January 6 (project 2021.1.01311.S). Given the precise photometric redshift estimate of COS-87259 ($z_{phot} = 6.83 \pm 0.06$; E22a), we used the band 6 receiver to target a frequency range of 239.42–244.79 GHz corresponding to $z_{[C\,II]} = 6.76$–6.94. During the ALMA observations, a total of 45 antennas were used in a configuration with baseline lengths spanning 15–977 m. The total integration time on COS-87259 was 33 min with an average precipitable water vapour level of 1.1 mm. The source J0948+0022 was used for calibration. We use the reduced data supplied by the observatory that were processed using CASA (McMullin et al. 2007) v.6.2.1.7 with pipeline v.2021.2.0.128. The resulting naturally weighted continuum-subtracted spectra have an rms sensitivity of ≈ 440 μJy per beam in 9.7 km s^{-1} channels, with a beam size of 0.49 arcsec by 0.37 arcsec and a position angle of $-76.6°$. The output continuum image ($\nu = 242.14$ GHz) has very similar beam properties with a size of 0.49 arcsec by 0.35 arcsec and a position angle of $-75.1°$, and reaches an rms sensitivity of 22 μJy per beam.

3 RESULTS

In this section, we begin by reporting the [C II]158 μm and underlying dust continuum data for COS-87259 (Section 3.1), summarizing the measured and derived properties in Table 1. We then compare the observed far-IR properties of COS-87259 to other known systems at $z > 6.5$ (Section 3.2). Finally, we quantify the relative positions of the far-IR, rest-UV, and radio emission, and subsequently investigate whether there is any evidence that source confusion is significantly impacting the mid-IR detections of COS-87259 (Section 3.3).

3.1 [C II]158 μm and dust continuum emission

The primary goal of our ALMA observations is to test the high-redshift ($z \simeq 6.83$) nature of COS-87259, as implied by the optical through sub-mm photometric spectral energy distribution (SED; E22a). We visually inspect the spectral data cubes, finding a clear
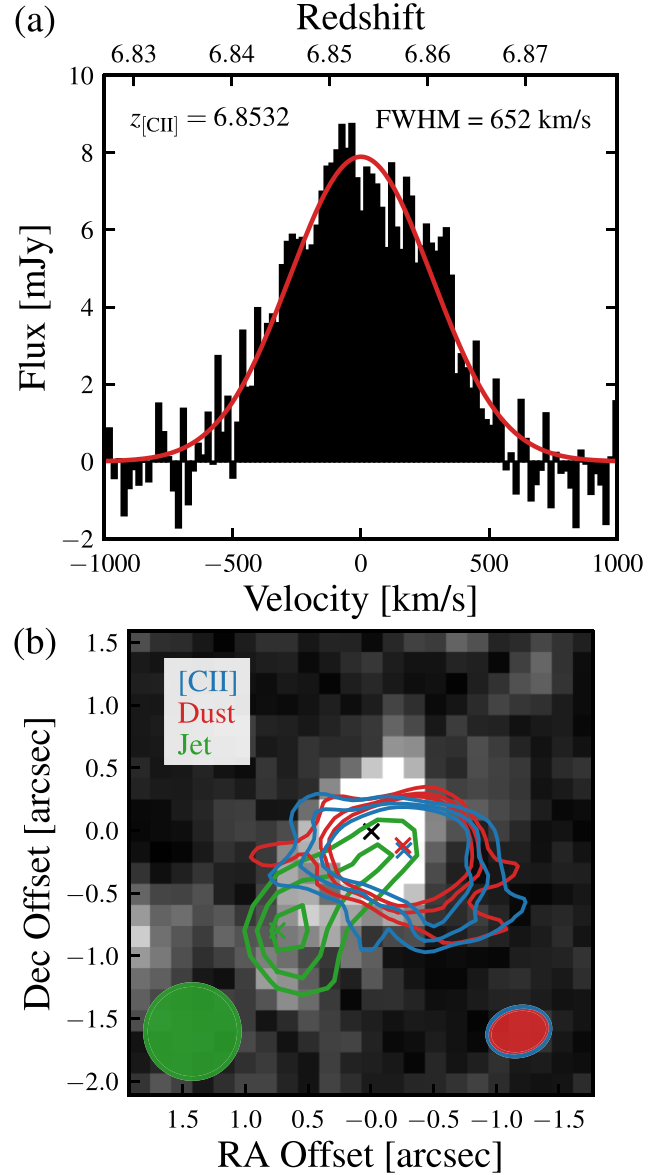
Table 1. Measured and derived properties of COS-87259. The reported [C II] and dust continuum sizes are the deconvolved values.

Rest-UV and radio properties (see E22a)	
UV right ascension	09:58:58.27
UV declination	+01:39:20.2
z_{phot}	6.83 ± 0.06
Rest-UV slope	-0.59 ± 0.27
M_{1450}	-21.7 ± 0.1
1.32–3 GHz radio slope	$-1.57^{+0.22}_{-0.21}$
0.144–1.32 GHz radio slope	$-0.86^{+0.22}_{-0.16}$
1.4 GHz luminosity	$(2.5 \pm 0.5) \times 10^{25}$ W Hz^{-1}
ALMA results	
$z_{[CII]}$	6.8532 ± 0.0002
[C II] FWHM	652 ± 17 km s^{-1}
[C II] size (core)	$(1.9 \pm 0.4$ kpc$) \times (<1.0$ kpc$^a)$
[C II] size (extended)	$(9.6 \pm 1.1$ kpc$) \times (4.9 \pm 0.6$ kpc$)$
$F_{[CII]}$ (core)	1.97 ± 0.16 Jy km s^{-1}
$F_{[CII]}$ (extended)	5.76 ± 0.64 Jy km s^{-1}
Total [C II] luminosity	$(8.82 \pm 0.75) \times 10^9$ L$_\odot$
Dust continuum size (core)	$(1.4 \pm 0.2$ kpc$) \times (1.0 \pm 0.1$ kpc$)$
Dust continuum size (extended)	$(7.8 \pm 10$ kpc$) \times (3.4 \pm 0.5$ kpc$)$
$F_{242\,GHz}$ (core)	1.48 ± 0.05 mJy
$F_{242\,GHz}$ (extended)	1.23 ± 0.15 mJy
Total $F_{242\,GHz}$	2.71 ± 0.16 mJy
$L_{IR,SF}^b$	$(8.7 \pm 0.5) \times 10^{12}$ L$_\odot$
M_{dust}^b	$(1.9 \pm 0.1) \times 10^9$ M$_\odot$
SFR$_{IR}^c$	1300 ± 70 M$_\odot$ yr^{-1}
SFR$_{[CII]}^d$	2970 ± 250 M$_\odot$ yr^{-1}
SED fitting results	
$L_{IR,AGN}$	$(2.5 \pm 0.2) \times 10^{13}$ L$_\odot$
$\tau_{9.7\,\mu m}$	2.3 ± 0.1
$L_{bol,AGN}$	$(5.1 \pm 0.5) \times 10^{13}$ L$_\odot$
$M_{1450,unobscured}$	-27.3 ± 0.1
$M_{BH} \lambda_{Edd}$	$(1.6 \pm 0.2) \times 10^9$ M$_\odot$
$L_{IR,SF}$	$(9.1 \pm 1.1) \times 10^{12}$ L$_\odot$
SFR	1610 ± 190 M$_\odot$ yr^{-1}
M_*	$(1.7 \pm 0.7) \times 10^{11}$ M$_\odot$

$^a 2\sigma$ upper limit on minor axis size from IMFIT..
^{b}Computed from the 158 μm dust continuum measurement adopting $T_{dust} = 47$ K and $\beta_{dust} = 1.6$.
^{c}Converted from $L_{IR,SF}$ using the relation of Murphy et al. (2011).
^{d}Converted from $L_{[CII]}$ using the relation of Herrera-Camus et al. (2015).

emission line detection coincident with the near-IR position of COS-87259. To generate a 1D spectrum of this emission line, we create a moment-0 map for the extraction. We determine the frequency range over which to make the moment-0 map by first extracting the (continuum-subtracted) spectra over a single beam centred on the rest-UV emission of COS-87259 and subsequently fitting a Gaussian profile to determine the line full width at half-maximum (FWHM) and central frequency. Following Schouws et al. (2022a), a moment-0 map is then generated by summing all channels that fall within ±FWHM determined above, and we next extract the spectrum within the 3σ contours and refit a Gaussian profile to determine the line FWHM and central frequency. This process is performed iteratively until the central frequency and FWHM converge (within a few iterations), which we then use to create the final moment-0 map and 1D extracted spectrum.

From a Gaussian fit to the final 1D spectrum (Fig. 1a), we measure an FWHM $= 652 \pm 17$ km s^{-1} and a central frequency of 242.009 ± 0.007 GHz. This central frequency corresponds to a [C II] redshift of $z_{[CII]} = 6.8532 \pm 0.0002$, in excellent agreement with the precise photometric redshift of $z_{phot} = 6.83 \pm 0.06$ set by

Figure 1. (a) ALMA [C II]158 μm spectrum of COS-87259 (after continuum subtraction) extracted within the 3σ contours of the moment-0 map. The spectrum is binned to half the original resolution for clarity and the red line shows the Gaussian fit. (b) ALMA [C II] (blue), 158 μm dust continuum (red), and VLA 3 GHz (green) 2σ, 3σ, and 4σ contour maps of COS-87259 overlaid on the stacked rest-UV image. The ALMA and VLA beams are shown in the bottom corners with their respective colours. The 3 GHz detection peak (green cross) is clearly offset (≈ 6 kpc projected) from the [C II] and dust continuum centroids (blue and red crosses), as expected if the radio emission is powered by an extended relativistic jet from the AGN. The centroid of the rest-UV emission (black cross) is also slightly offset from that of the far-IR (≈ 1.5 kpc), consistent with strong dust opacity variations across the galaxy.

the sharp spectral break seen between the Subaru/Hyper Suprime-Cam intermediate/narrow bands at 9450 and 9700 Å (E22a). We therefore conclude that the ALMA-detected emission feature seen from COS-87259 is the [C II]158 μm line.

The [C II] emission of COS-87259 is spatially resolved with our moderate-resolution (beam ≈ 0.4 arcsec) ALMA data (Fig. 1b). To determine the flux and size of the [C II] emission, we use the CASA task IMFIT that fits one or more 2D Gaussians to the moment-0

map. We find that a single elliptical Gaussian poorly reproduces the observed [C II] surface brightness profile, while a two-component model provides a satisfactory match to the data (Fig. 2). This two-component fit suggests the presence of a compact ($\approx$2 kpc) [C II]-emitting core in addition to a more extended ($\approx$10 kpc) region of emission, consistent with the [C II] surface brightness profiles of $z >$ 6 quasar hosts (Novak et al. 2020). The extended [C II] component of COS-87259 has a deconvolved size of (1.82 $\pm$ 0.21 arcsec) $\times$ (0.93 $\pm$ 0.11 arcsec) and an integrated flux of 5.76 $\pm$ 0.64 Jy km s^{-1}. At the [C II] redshift of COS-87259 ($z_{[CII]} = 6.853$), these values translate to a physical size and [C II] line luminosity of (9.6 $\pm$ 1.1 kpc) $\times$ (4.9 $\pm$ 0.6 kpc) and (6.57$\pm$0.73) $\times$ 10^9 L$_\odot$, respectively. The compact component is only resolved along the major axis with an estimated deconvolved size of 0.35 $\pm$ 0.07 arcsec (1.9 $\pm$ 0.4 kpc) and its integrated flux is found to be 1.97 $\pm$ 0.16 Jy km s^{-1}, which corresponds to a luminosity of (2.25$\pm$0.18) $\times$ 10^9 L$_\odot$. The two-component IMFIT output therefore implies a total [C II] luminosity of (8.82$\pm$0.75) $\times$ 10^9 L$_\odot$, the bulk of which is originating from the extended component (75 $\pm$ 10 per cent).

The [C II] emission line is frequently used as a valuable tracer of the interstellar medium kinematics for reionization-era galaxies (e.g. Smit et al. 2018; Hashimoto et al. 2019; Matthee et al. 2019; Neeleman et al. 2019). We begin investigating the kinematics of COS-87259 by generating maps of the [C II] mean velocity and velocity dispersion fields using the code QUBEFIT (Neeleman et al. 2021). When running QUBEFIT, we apply a 1σ clipping as a compromise between mitigating the impact of noise on the resulting moment maps while preserving true signal (see discussion in Neeleman et al. 2021). We have verified that our conclusions do not significant change if we instead adopt a clipping threshold in the range of 0.5σ–2σ. A prominent gradient is found in the mean velocity field with a maximum difference of $\approx$360 km s^{-1} between spaxels in the north-east and south-west corners (Fig. 3). The velocity dispersion map also shows that the outermost spaxels tend to have a larger fitted FWHM ($\sim$600–900 km s^{-1}) than those located near the peak of emission ($\approx$550 km s^{-1}; see Fig. 3). This perhaps suggests the presence of a broader [C II] wing in COS-87259 as reported in other $z >$ 6 AGN hosts (Maiolino et al. 2012; Izumi et al. 2021) and stacked spectra of $z = 4$–6 galaxies (Ginolfi et al. 2020), implying significant outflowing gas. However, because the [C II] FWHM only varies by a factor of $\approx$1.5 across COS-87259 (cf. the factor of 4 in Izumi et al. 2021), it is much more challenging to determine whether a broad wing is indeed present in this system with existing moderate-resolution data. Upon extracting the [C II] spectrum across the outermost spaxels in the moment-0 footprint, we find that the resulting profile has a slightly larger fitted FWHM (690$^{+60}_{-50}$ km s^{-1}), though consistent with the full profile shown in Fig. 1(a) within uncertainties. We also extract position–velocity information along the major axis (as determined by a single 2D Gaussian fit) and find no clear evidence of multiple distinct components separated in velocity space (see Fig. A1). Higher resolution [C II] data will be required to better assess whether the kinematics of COS-87259 are more consistent with a rotating disc or a disturbed, possibly merging system.

Strong dust continuum emission is also detected from COS-87259 (Fig. 1b). Similar to the [C II] emission, we find that the dust continuum surface brightness profile is much better fitted by the superposition of two elliptical Gaussians as opposed to a single Gaussian (Fig. 2). With IMFIT, we find a deconvolved angular size of (1.47 $\pm$ 0.19 arcsec) $\times$ (0.65 $\pm$ 0.10 arcsec) and (0.26 $\pm$ 0.03 arcsec) $\times$ (0.18 $\pm$ 0.02 arcsec) for the more extended and compact components, respectively. These scales correspond to physical sizes of (7.8 $\pm$ 1.0 kpc) $\times$ (3.4 $\pm$ 0.5 kpc) and (1.4 $\pm$ 0.2 kpc)

$\times$ (1.0 $\pm$ 0.1 kpc), respectively, which are systematically $\approx$20–30 per cent smaller than those found for the [C II] emission. The integrated flux densities of the more compact and extended components are nearly equal at 1.48 $\pm$ 0.05 and 1.23 $\pm$ 0.15 mJy, respectively, yielding a total 158 μm dust continuum flux density of 2.71 $\pm$ 0.16 mJy for COS-87259.
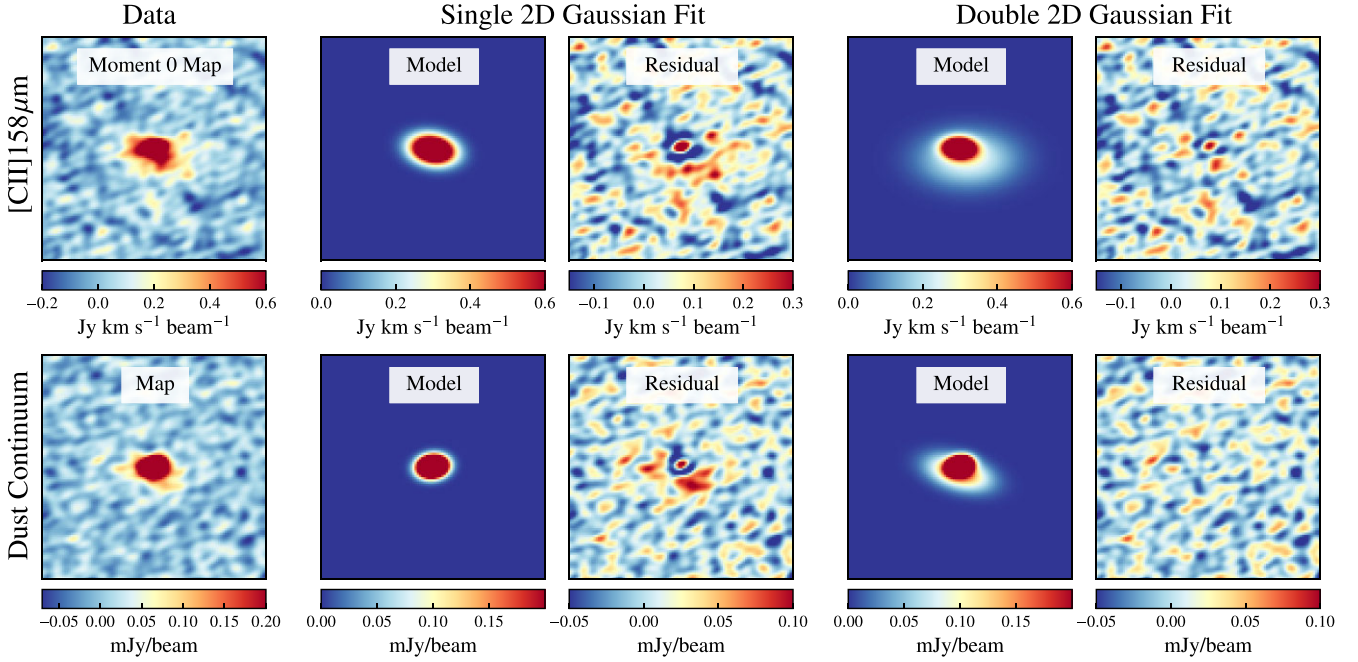
Given the highly luminous nature of COS-87259, we investigate whether this system may be significantly magnified by nearby foreground objects. We consider all foreground objects within 10 arcsec of COS-87259 identified in the COSMOS2020 catalogue (Weaver et al. 2022), assuming each is a singular isothermal sphere with photometric redshift and stellar mass taken from that same catalogue. The velocity dispersion of each neighbouring source is computed in two independent ways. First, we assume that each galaxy occupies a virialized halo with 200$\times$ the mean density of the Universe at its assumed redshift and mass 100$\times$ that of the stellar mass. Our second approach follows that of Mason, Trenti & Treu (2015) where we adopt the relation between velocity dispersion and stellar mass from Auger et al. (2010). Both methods to estimate velocity dispersions suggest that COS-87259 is only weakly lensed by neighbouring foreground sources, with a small combined magnification factor of $\mu_{tot} \approx$ 1.15–1.25. Because this weak magnification does not significantly impact our main conclusions, we choose not to correct for it when reporting the measured and inferred properties of COS-87259.

3.2 Comparison of far-IR properties to other $z >$ 6.5 sources

We compare the observed far-IR properties ([C II] luminosity, [C II] FWHM, and monochromatic 158 μm dust continuum luminosity) of COS-87259 to other known objects in the reionization era. From the literature, we compile such measured properties from known $z >$ 6.5 sub-mm galaxies (Strandet et al. 2017; Marrone et al. 2018), extremely UV-luminous quasars ($M_{UV} \leq -25$; Venemans et al. 2012, 2016, 2017b; Bañados et al. 2015; Mazzucchelli et al. 2017; Decarli et al. 2018; Yang et al. 2019b, 2020b; Wang et al. 2021; Yue et al. 2021), UV-bright Lyman-break galaxies ($M_{UV} \leq -21$; Pentericci et al. 2016; Smit et al. 2018; Hashimoto et al. 2019; Bouwens et al. 2022; Inami et al. 2022; Schouws et al. 2022a, b), reddened type 1 quasars (Izumi et al. 2021; Fujimoto et al. 2022), and companion galaxies serendipitously identified from ALMA observations (Decarli et al. 2017; Willott, Bergeron & Omont 2017; Neeleman et al. 2019; Venemans et al. 2019, 2020; Fudamoto et al. 2021). We correct the properties of the sub-mm system SPT0311-58 and the quasar J0439+1634 for strong gravitational lensing given reported magnification factors (Marrone et al. 2018; Yue et al. 2021).

With a [C II] luminosity of (8.82$\pm$0.75) $\times$ 10^9 L$_\odot$, COS-87259 is the second most [C II] luminous object known at $z >$ 6.5 (Fig. 4a), being outshined by only the sub-mm galaxy SPT0311-58W at $z =$ 6.900 (1.02$\times$10^{10} L$_\odot$). The [C II] line of COS-87259 is nearly 5$\times$ brighter than typical extremely bright $z >$ 6.5 quasars (median $L_{[CII]} = 2.0 \times 10^9$ L$_\odot$) and 16$\times$ brighter than typical UV-bright Lyman-break $z >$ 6.5 galaxies (median $L_{[CII]} = 0.55 \times 10^9$ L$_\odot$). COS-87259 additionally shows a [C II] line that is 4.7–8.0$\times$ brighter than the two reddened type 1 quasars thus far identified at $z >$ 6.5 (Izumi et al. 2021; Fujimoto et al. 2022).

The [C II] line width of COS-87259 (FWHM = 652 $\pm$ 17 km s^{-1}) is also exceptionally broad for known systems at $z >$ 6.5 (Fig. 4b), only surpassed by SPT0311-58W (FWHM = 840 $\pm$ 10 km s^{-1}; Marrone et al. 2018) and the $z =$ 6.66 quasar PSO J338+29 (FWHM = 740$^{+540}_{-310}$ km s^{-1}; Mazzucchelli et al. 2017). For reference, the typical [C II] line widths of extremely UV-luminous $z >$ 6.5 quasars

Figure 2. Illustration of the 2D Gaussian fits to the [C II] moment-0 map (top) and the 158 μm dust continuum map (bottom). The data are shown in the leftmost panels, with the best-fitting single elliptical Gaussian models shown in the second panels from left. These single Gaussian fits provide a poor match to the measured surface brightness profiles of both the [C II] and dust continuum data, as can be seen by the strong residuals in the middle panels. The data are much better fitted as the superposition of two elliptical Gaussians as illustrated in the two rightmost panels. Each panel is 7.3 arcsec (39 kpc) on a side.

and Lyman-break galaxies are 2.0 and 2.7× narrower than that of COS-87259, respectively. Finally, we note that the monochromatic 158 μm dust continuum luminosity of COS-87259 [$(9.3 \pm 0.5) \times 10^{11}$ L$_\odot$] is among the brightest of any known object at $z > 6.5$ (Fig. 4c). This 158 μm continuum luminosity is very similar to that of $z > 6.5$ quasars, with only SPT0311-58W substantially outshining COS-87259 in the continuum around [C II]. While the conversion between 158 μm luminosity to total IR luminosity depends on dust temperature and emissivity, it is none the less clear that COS-87259 is among the most extreme objects known in the reionization era in terms of its observed [C II] and dust continuum properties. This suggests that COS-87259 is likely one of the most massive galaxies at $z \sim 7$ with a very large star formation rate, as supported by the full near-IR to millimetre SED of this system (see Section 4).

3.3 Relative positions of the multiwavelength emission

To further characterize COS-87259, we compare the relative positions of the [C II], dust continuum, rest-UV, and radio emission, all of which are imaged with FWHM ≈ 0.4–0.8 arcsec (≈2–4 kpc) resolution. The centroids of the [C II] and dust continuum emission are consistent within uncertainties ($\Delta\theta = 0.04 \pm 0.03$ arcsec), indicating that the 158 μm dust continuum is concentrated near the dynamical centre of the galaxy. Here, we have computed 1σ positional uncertainties from the ALMA data as[1] (beam FWHM)/(peak S/N)/0.9, enforcing a minimum positional uncertainty of $\sigma_{\mathrm{min}} =$ (beam FWHM)/20/0.9 due to limits imposed by atmospheric phase fluctuations. We also find that the 3 GHz radio emission peak from COS-87259 (beam = 0.75
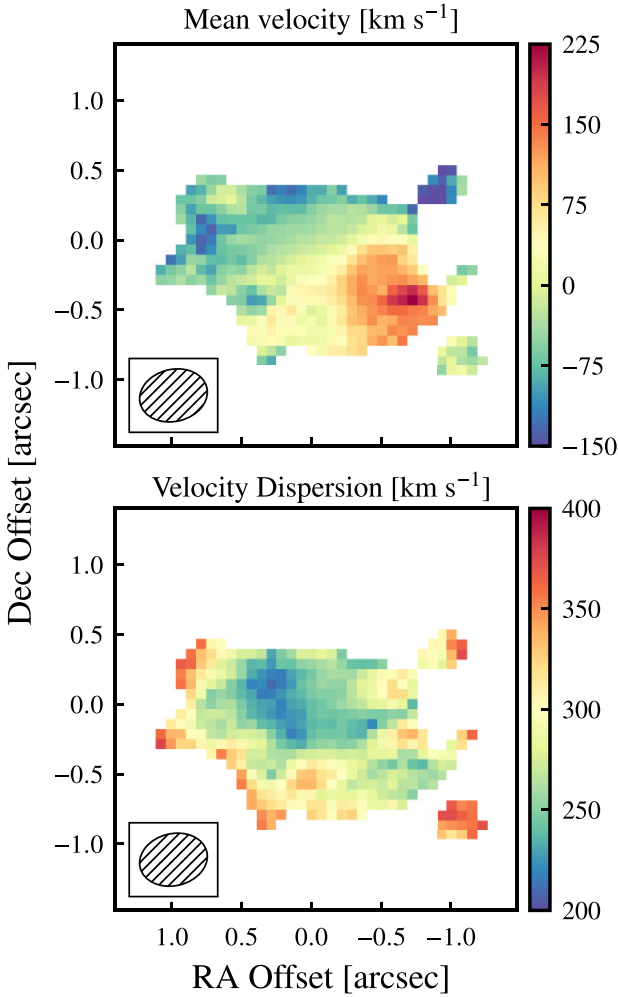
arcsec; Smolčić et al. 2017) is significantly offset from the dust continuum centroid with a separation of 1.21 ± 0.17 arcsec (see Fig. 1b). This large (6.4 ± 0.9 kpc projected) offset is to be expected if the radio emission seen from COS-87259 is powered by an extended relativistic jet emerging from the AGN.

The rest-UV emission centroid from COS-87259 also appears slightly offset from both the [C II] and dust continuum centroids (Fig. 1b). We measure the rest-UV centroid from a stack of the Hyper Suprime-Cam Subaru Strategic Program (HSCSSP) public data release 2 (PDR2) *y* and UltraVISTA data release 4 (DR4[2]) *Y*, *J*, *H*, and *K$_s$* images, each of which has a seeing-limited FWHM of ≈0.77 arcsec and is calibrated to the *Gaia* astrometric frame with an absolute position uncertainty of ≤0.05 arcsec (McCracken et al. 2012; Aihara et al. 2019). The stacked rest-UV detection of COS-87259 has an S/N = 15, suggesting a relative positional uncertainty of FWHM/(S/N) ≈ 0.05 arcsec, comparable to the absolute precision. To be conservative, we adopt a total position uncertainty of 0.10 arcsec for the rest-UV emission. This results in a total offset of 0.30 ± 0.10 arcsec between the rest-UV and [C II] emission centroids, as well as a very similar offset from the dust continuum. Such moderate (~1–2 kpc) offsets between the dust continuum and rest-UV centroids have been found among other UV-bright Lyman-break $z \sim 7$ galaxies and are often coupled with strong spatial gradients in the rest-UV slope, indicating considerable dust opacity variations across the galaxy (e.g. Carniani et al. 2018; Bowler et al. 2022).

COS-87259 is also detected at a fairly high S/N ($\sim 10\sigma$–20σ) in the *Spitzer*/IRAC 3.6 μm, 4.5 μm, and MIPS 24 μm bands (see Fig. 5; E22a). Given the relatively poor angular resolution of the *Spitzer* images (FWHM ≈ 1.8–6 arcsec), we investigate whether there is
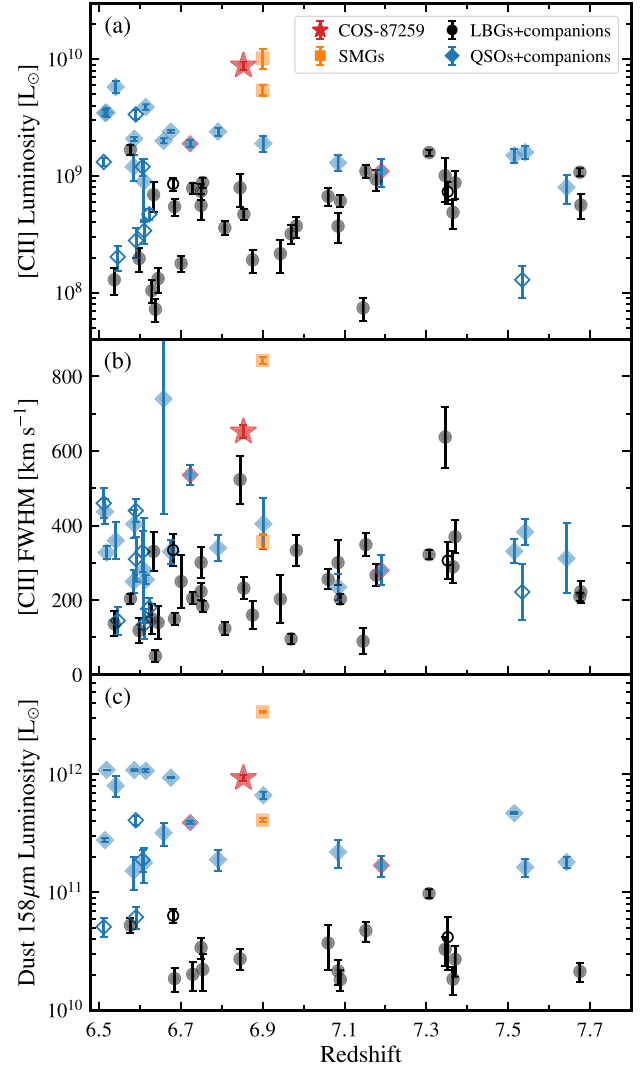
Figure 3. Maps of the [C II] mean velocity (top) and velocity dispersion (bottom) fields of COS-87259 derived using QUBEFIT. The footprint of each map is confined to pixels with $>3\sigma$ [C II] flux and the [C II] beam (≈ 0.4 arcsec) is shown in the bottom left corner of each panel. A prominent gradient is seen in the mean velocity field and there is evidence of larger velocity dispersion towards the outer edges of the [C II] emission.
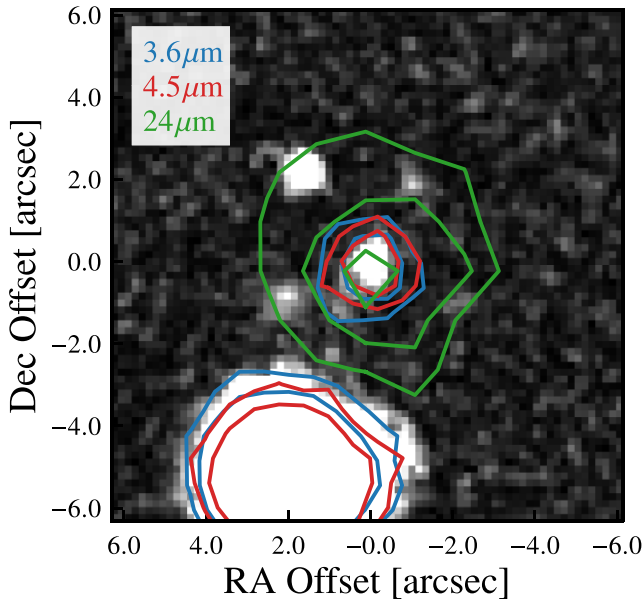

Figure 4. Comparison of the observed far-IR properties of COS-87259 with other known objects at $z > 6.5$. We compare the [C II] luminosity, [C II] FWHM, and monochromatic 158 μm dust continuum luminosities in panels (a), (b), and (c), respectively. A full description of the objects shown in this plot is provided in Section 3.2. The two known red type 1 quasars at $z > 6.5$ are shown as blue diamonds with red edges. Serendipitously detected companions of quasars and Lyman-break galaxies are shown as empty markers. We correct for strong gravitational lensing where appropriate.

any evidence that these detections are significantly impacted by confusion. After calibrating the *Spitzer* images to the *Gaia* astrometric frame (using the IRAF task CCMAP), we find that the centroids of all detections are closely aligned with the rest-UV centroid of COS-87259 ($\Delta\theta < 0.5$ arcsec). Moreover, none of the *Spitzer* contours show any sign of strong asymmetry (see Fig. 5). The next nearest MIPS 24 μm detection is 12 arcsec (i.e. $2\times$ the FWHM) away from COS-87259, while the next nearest strong IRAC detection is from an object 5.4 arcsec away (i.e. $3\times$ the FWHM) located at the bottom of Fig. 5. Overall, we find no evidence that nearby objects are contributing significantly to the *Spitzer* detections of COS-87259. None the less, the IRAC, MIPS, PACS, and SPIRE photometry of COS-87259 used below were all computed after performing deconfusion using the relatively high resolution imaging as a prior (see E22a for further details).

4 THE PHYSICAL PROPERTIES OF COS-87259

Now equipped with measurements of the [C II] systemic redshift and 158 μm dust continuum emission, we reassess the inferred physical properties of COS-87259 derived in E22a. To start, we fit the observed near-IR to millimetre SED of COS-87259 using a custom Bayesian SED fitting package (Lyu et al. 2022) that utilizes dynamic nested sampling (DYNESTY; Speagle 2020) and feature (semi-)empirical templates of AGN and star-forming dust emission. The validity of this tool has been demonstrated by finding and characterizing obscured AGNs within the GOODS-S field in Lyu et al. (2022), and we refer the interested reader to that paper as well as Lyu & Rieke (2022, their section 4.2) for details of this code. For the purposes of this work, we adopt the Lyu, Rieke & Shi (2017) warm-dust-deficient AGN SED (which is suitable for very luminous AGNs like COS-87259; see below) and account for
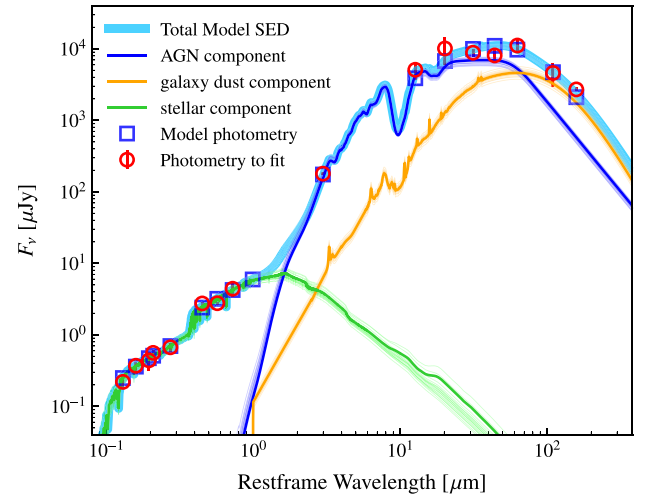
Figure 5. Figure showing the *Spitzer*/IRAC 3.6 μm (blue), 4.5 μm (red), as well as *Spitzer*/MIPS 24 μm (green) emission around COS-87259. We show 7σ and 12σ contours for IRAC, and 4σ, 6σ, and 8σ contours for MIPS. The background image is the near-IR stack centred on the rest-UV position of COS-87259. The centroids of each *Spitzer* detection near COS-87259 are closely aligned with the rest-UV centroid (<0.5 arcsec) and there is no evidence of significant confusion impacting any of the *Spitzer* detections.

obscuration using an empirical AGN IR attenuation curve (Lyu & Rieke 2022). The galaxy dust emission is represented by the IR SED template of Haro 11 that successfully matches the observed IR SEDs and expected physical properties of massive $5 < z < 7$ galaxies (De Rossi et al. 2018), including the hosts of $z > 5$ quasars (Lyu, Rieke & Alberts 2016). Along with these AGNs and galaxy dust emission components, we include stellar emission using the flexible stellar population synthesis (FSPS) code (Conroy, Gunn & White 2009; Conroy & Gunn 2010) under the SED fitting framework provided by PROSPECTOR (Johnson et al. 2021). For this stellar emission, we adopt a delayed star formation history, a Calzetti et al. (2000) attenuation curve (as is likely appropriate for a dust and hence metal-rich system like COS-87259; e.g. Shivaei et al. 2020), and a Kroupa (2001) stellar initial mass function.

In the SED fitting procedure, we include all VISTA Infrared Camera (VIRCam), Wide Field Camera 3 (WFC3), IRAC, MIPS, PACS, SPIRE, and SCUBA-2 photometry of COS-87259 (see table 1 of E22a) as well as the 158 μm dust continuum measurement from our new ALMA data. The only difference from the photometry adopted in E22a is that we here use the deboosted SCUBA-2 850 μm flux density measurement of 4.60 ± 1.65 mJy (Simpson et al. 2019). The IRAC, MIPS, PACS, and SPIRE photometry were all computed using deconfusion algorithms (see E22a). We note that the reported uncertainties on inferred physical properties below are largely dominated by the statistical uncertainties from the photometric measurements and do not include systematic uncertainties arising from our adopted set of SED templates. Using the X-CIGALE SED-fitting code (Yang et al. 2020a) as described in E22a, we infer similar values for the physical parameters (within $\lesssim 0.3$ dex).

Before reporting the results from our SED fit, we briefly discuss the photometric properties of COS-87259 to provide context on what is driving the inferred physical parameters (see E22a for further details).

Figure 6. Near-IR through millimetre SED of COS-87259. The photometric data (see E22a) and ALMA band 6 continuum measurement are shown as red circles with the best-fitting SED and its corresponding model photometry shown via a thick, light blue line and blue squares, respectively. We also show the relative contributions of the stellar, AGN, and (star-forming) dust emission as green, blue, and gold lines, respectively. The transparent lines show 20 realizations of the fit randomly sampled from the output posterior distribution to illustrate the fitting uncertainties. COS-87259 is inferred to be an extremely massive reionization-era galaxy harbouring a heavily obscured luminous AGN and powering intense dust-obscured star formation.

From the VIRCam photometry, COS-87259 shows an extremely red rest-UV slope ($\beta = -0.6$ where $f_\lambda \propto \lambda^\beta$) compared to typical UV-bright $z \sim 7$ Lyman-break galaxies ($\beta \approx -1.8$; Bowler et al. 2017; Endsley et al. 2021a), indicating unusually strong dust attenuation. At slightly redder wavelengths, COS-87259 shows a jump in flux density between the K_s (0.67 ± 0.09 μJy) and IRAC $3.6 + 4.5$ μm bands (≈ 2.75 μJy) that is much stronger than expected from extrapolating the rest-UV slope, consistent with a prominent Balmer break. The flux density then steeply rises between the IRAC 8 μm (<4.9 μJy 2σ), MIPS 24 μm (180 ± 6 μJy), and PACS 100 μm (5100 ± 1400 μJy) bands, as would be expected from hot dust emission powered by a highly obscured AGN. Finally, we note that COS-87259 shows a relatively flat and bright SED between the PACS, SPIRE, and SCUBA-2 160–850 μm bands (≈ 5–10 mJy in each filter), indicative of very luminous hot (AGN powered) and warm (star formation powered) dust emission, the latter of which is now corroborated by the strong ALMA 158 μm continuum detection. As discussed in E22a, the MIPS, PACS, SPIRE, and SCUBA-2 photometry of COS-87259 are consistent with the SEDs of hot dust-obscured galaxies identified at lower redshifts (e.g. Eisenhardt et al. 2012; Tsai et al. 2015; Fan et al. 2016).

From the SED fit (see Fig. 6), COS-87259 is inferred to harbour a very luminous AGN [$L_{\rm IR,AGN} = (2.5 \pm 0.2) \times 10^{13}$ L$_\odot$] that is heavily obscured with an optical depth at rest-frame 9.7 μm of $\tau_{9.7\,\mu m} = 2.3 \pm 0.1$. Such inferred obscuration is consistent with Compton-thick absorption ($N_H \gtrsim 10^{24}$ cm^{-2}; Shi et al. 2006) and helps explain the weak X-ray luminosity of COS-87259, which remains undetected in the 160 ks *Chandra* imaging over COSMOS (Civano et al. 2016; see E22a for further details). Using the Runnoe, Brotherton & Shang (2012) bolometric conversion from rest-frame 5100 Å luminosity, the intrinsic (de-reddened) AGN SED implied by our fits suggests a bolometric AGN luminosity of $L_{\rm bol,AGN} = (5.1 \pm 0.5) \times 10^{13}$ L$_\odot$. Such a large bolometric AGN luminosity is comparable to that of $z \sim$

1–4 hot dust-obscured galaxies (e.g. Eisenhardt et al. 2012; Tsai et al. 2015; Fan et al. 2016) as well as $z \sim 7$ quasars (e.g. Mazzucchelli et al. 2017; Yang et al. 2021), and implies a black hole mass of $M_{BH} = (1.6 \pm 0.2) \times 10^9 \, M_\odot / \lambda_{Edd}$ for COS-87259, where λ_{Edd} is the Eddington ratio. We come back to discuss potential implications of identifying such an early supermassive black hole over a relatively small area (1.5 deg^2) at the end of this section.

Due to the strong jump in flux density between the VIRCam K_s and IRAC bands, the rest-UV + optical emission of COS-87259 is inferred to be powered by star formation (with a prominent Balmer break) rather than by the AGN (Fig. 6). To further assess whether the rest-UV + optical photometry of COS-87259 may plausibly be due to reddened AGN emission, we also compare these data to empirical spectra of lower redshift quasars. Specifically, we fit the VIRCam Y, J, H, and K_s as well as the IRAC 4.5 μm photometry of COS-87259 to the composite $z \sim 1.5$ blue quasar spectrum from Selsing et al. (2016) after redshifting to $z = 6.853$ and applying a range of V-band optical depths ($0 < A_V < 2$) using the Small Magellanic Cloud (SMC) attenuation law (Pei 1992) motivated by previous studies of red quasars (e.g. Richards et al. 2003; Hopkins et al. 2004). In this fit, we do not include the 3.6 μm band as it can be contaminated by strong [O III] + Hβ emission at the redshift of COS-87259. This fitting procedure results in a best-fitting reduced $\chi^2 = 11.8$ with $3\sigma - 6\sigma$ offsets in the K_s and 4.5 μm bands, indicating that the rest-UV + optical photometry of COS-87259 is poorly explained by such AGN spectra. Ultimately, UV + optical spectra of COS-87259 (taken with e.g. *JWST*/NIRSpec) will be necessary to determine the physical origin of this emission.

Assuming that the UV + optical emission is dominated by star formation, the fiducial SED fit shown in Fig. 6 returns a total stellar mass of $M_* = (1.7 \pm 0.7) \times 10^{11} \, M_\odot$, implying that COS-87259 is an extremely massive $z \sim 7$ galaxy as perhaps expected given its extreme far-IR properties (Fig. 4). However, as discussed elsewhere (van Mierlo, Caputi & Kokorev 2022a; Whitler et al. 2023; see also E22a), alternative assumptions to the star formation history can yield significantly lower stellar mass estimates for COS-87259 [$M_* \sim (1 - 3) \times 10^{10} \, M_\odot$] wherein the strong jump in flux density between K_s and [3.6] is inferred to be strongly assisted by prominent [O III] + Hβ emission. None the less, the full range of estimated stellar masses for COS-87259 ($\sim 10^{10-11} \, M_\odot$) still falls substantially below that expected given local relations between the properties of supermassive black holes and their host galaxies. With an inferred black hole mass of $\sim 1.5 \times 10^9 \, M_\odot$, the relation of Häring & Rix (2004) predicts a stellar mass of $\sim 10^{12} \, M_\odot$ for COS-87259. Similar inferred offsets towards higher black hole mass at fixed galaxy mass have been reported for luminous high-redshift quasars (e.g. Trakhtenbrot et al. 2015; Venemans et al. 2016; Pensabene et al. 2020) as well as hot dust-obscured galaxies (Assef et al. 2015; Tsai et al. 2015), potentially indicating that the growth of their supermassive black holes outpaced that of the host galaxies at early times.

The models also suggest that intense obscured star formation within COS-87259 is powering a total (8–1000 μm rest-frame) IR luminosity of $L_{IR,SF} = (9.1 \pm 1.1) \times 10^{12} \, L_\odot$, with a corresponding very large star formation rate (SFR) of $1610 \pm 190 \, M_\odot \, yr^{-1}$. For comparison, we also derive the obscured star formation properties of COS-87259 adopting the standard approach for $z > 6$ quasars. In these objects, the dust emission is often assumed to follow a modified blackbody with temperature $T = 47$ K and emissivity index $\beta = 1.6$ (e.g. Beelen et al. 2006; Decarli et al. 2018; Venemans et al. 2020). After fixing the SED normalization to match the 158 μm dust continuum measurement of COS-87259, this approach yields an IR luminosity and obscured star formation rate (Murphy et al. 2011)

of $(8.7 \pm 0.5) \times 10^{12} \, L_\odot$ and $1300 \pm 70 \, M_\odot \, yr^{-1}$, respectively, similar to that obtained from the SED fit using the Haro 11 template. The modified blackbody fit also implies a very large dust mass of $M_{dust} = (1.9 \pm 0.1) \times 10^9 \, M_\odot$. Finally, we note that if we adopt the SFR–$L_{[C II]}$ conversion of Herrera-Camus et al. (2015), we infer a total star formation rate of $2970 \pm 250 \, M_\odot \, yr^{-1}$. While this [C II]-based SFR is $2.3\times$ larger than that inferred from the dust SED, we note that there remain considerable uncertainties on both the dust temperature and emissivity index for COS-87259. Regardless, the very bright ALMA detections of COS-87259 make it clear that this object is undergoing vigorous obscured star formation activity comparable to $z \sim 7$ sub-mm galaxies and quasar hosts (Fig. 4). The range of stellar masses ($\sim 10^{10-11} \, M_\odot$) and SFRs (1300–3000 $M_\odot \, yr^{-1}$) inferred for COS-87259 suggest a specific SFR (sSFR) between 13 and 300 Gyr^{-1}, consistent with the range of sSFRs inferred among otherwise typical extremely UV-luminous ($M_{UV} \sim -22$) $z \sim 7–8$ galaxies (Topping et al. 2022). Additional data will be required to determine whether the AGN within COS-87259 is significantly impacting its star formation efficiency.

With an inferred bolometric AGN luminosity of $\sim 5 \times 10^{13} \, L_\odot$, the supermassive black hole within COS-87259 is comparable to that powering the brightest quasars known at $z > 6$ (e.g. Yang et al. 2021) that are discovered using extremely wide-area ($\gtrsim 1000$ deg^2) surveys. The identification of COS-87259 within the relatively small 1.5 deg^2 COSMOS field is therefore very surprising. To better place COS-87259 into context of the UV-luminous quasar population, we extract its de-reddened rest-frame 1450 Å AGN luminosity from the SED fit described in Section 4. This suggests that COS-87259 is a highly obscured version of an $M_{1450} \approx -27.3$ quasar that, at $z \sim 7$, has been found to be powered by $\approx 1.5 \times 10^9 \, M_\odot$ black holes accreting near the Eddington limit (Yang et al. 2021). Such UV-luminous quasars ($M_{1450} \leq -27$) are an exceedingly rare population in the very early Universe with a surface density of ≈ 1 per 3000 deg^2 at $z = 6.6–6.9$ (Wang et al. 2019), the approximate redshift interval over which COS-87259 was selected. While COS-87259 is only one object and thus may have simply been a fortuitous discovery, we briefly discuss what the spectroscopic confirmation of this object may imply for the assembly of supermassive black holes at $z \gtrsim 7$. We refer the interested reader to section 4.2 of E22a for a more extended discussion of what COS-87259 may imply for the statistical properties of UV-bright ($M_{UV} \lesssim -21.25$) massive ($M_* > 10^{10} \, M_\odot$) $z \sim 7$ galaxies, as well as the possible contribution of this population to the obscured star formation rate density at early times.

The identification of COS-87259 within the 1.5 deg^2 COSMOS field versus the very low surface density of similarly luminous $z \sim 6.8$ quasars ($\approx 1/3000$ deg^{-2}; see above) raises the question of whether rest-UV selections may be missing a very large fraction ($\gtrsim 1000\times$) of heavily obscured black hole growth in the early Universe. Observations of both the local Universe and the $z > 6$ quasar population provide some insight. The known population of early UV-luminous quasars suggests that approximately 0.1 per cent of the total black hole mass density inferred at present day had already formed by $z = 6$ (e.g. Marconi et al. 2004; Shen et al. 2020). Therefore, boosting the total black hole mass density at $z > 6$ by a factor of $\gtrsim 1000$ (to correct for an extremely dominant population of heavily obscured AGNs) would imply little cosmic black hole growth between $0 < z < 6$. Such a scenario is inconsistent with the census of AGN activity at these redshifts (Shen et al. 2020). This line of reasoning suggests that it is unlikely that there are $\gtrsim 3$ orders of magnitude more buried AGNs at $z > 6$ than expected based on results from rest-UV-selected samples.

However, it remains unknown whether the most massive ($\sim 10^9 \, M_\odot$) black holes at $z \gtrsim 7$ very frequently grew in heavily obscured phases. Indirect evidence for such a scenario has emerged in recent years, with spectroscopic observations showing that a large fraction of UV-luminous $z > 6$ quasars possess much smaller Lyα proximity zones than expected given their black hole masses (Davies et al. 2019; Eilers et al. 2020, 2021). Even though these early supermassive black holes have presumably been growing for several hundred million years (Inayoshi, Visbal & Haiman 2020), their proximity zones imply that they have only been ionizing their surrounding IGM for $\sim 10^6$ yr on average (Morey et al. 2021). This apparent tension can be alleviated if the supermassive black holes powering $z > 6$ quasars were heavily obscured for a large fraction ($\gtrsim 95$ per cent) of their lifetime (Eilers, Hennawi & Davies 2018; Davies et al. 2019). However, it is not clear what physical mechanism might drive such a very dominant population of heavily obscured luminous AGNs at $z \gtrsim 7$ given that X-ray observations imply an obscured ($N_H > 10^{23}$ cm^{-2}) fraction of ~ 80 per cent among luminous ($L_{bol} \sim 10^{13} \, L_\odot$) AGNs at $z \sim 3$–6 (Vito et al. 2018). One potential contributing factor could be the increasing gas and dust density within massive galaxies towards higher redshifts (Circosta et al. 2019), as suggested by recent hydrodynamic simulations (Trebitsch et al. 2019; Ni et al. 2020; Lupi et al. 2022). Ultimately, wider area searches for very luminous ($L_{bol} \gtrsim 10^{13} \, L_\odot$) heavily obscured AGNs at $z > 6$ will be required to better assess how common this population is relative to quasars, with subsequent detailed follow-up necessary to characterize the origin of their obscuration.

5 SUMMARY AND OUTLOOK

In this work, we have reported the results of ALMA follow-up observations targeting the [C II]158 μm line and underlying dust continuum from a previously reported candidate heavily obscured radio-loud ($L_{1.4\,GHz} = 10^{25.4}$ W Hz^{-1}) AGN at $z \simeq 6.83$ identified in the 1.5 deg^2 COSMOS field (COS-87259; E22a). Our summary and conclusions are listed below:

(i) The ALMA data confidently reveal a luminous emission line with a central frequency of 242.009 ± 0.007 GHz coincident with the near-IR position of COS-87259 (Fig. 1). We conclude that this emission feature is the [C II]158 μm cooling line at $z_{[CII]} = 6.8532 \pm 0.0002$, which is in excellent agreement with the precise photometric redshift of COS-87259 ($z_{phot} = 6.83 \pm 0.06$) set by the sharp Lyman-alpha break seen between two narrow/intermediate bands at 9450 and 9700 Å (E22a).

(ii) The [C II]158 μm emission of COS-87259 is spatially resolved with our moderate-resolution (beam ≈ 0.4 arcsec) ALMA data and its surface brightness profile suggests the presence of a compact (major axis $= 1.9 \pm 0.4$ kpc) [C II]-emitting core in addition to a more extended (major axis $= 9.6 \pm 1.1$ kpc) region of emission (Fig. 2), similar to that of $z > 6$ quasar hosts (Novak et al. 2020). Summing the two emission components, we measure a total [C II] line luminosity of $(8.82 \pm 0.75) \times 10^9 \, L_\odot$ from COS-87259, the bulk of which is originating from the more extended region (75 ± 10 per cent). The [C II] emission is extremely broad (FWHM $= 652 \pm 17$ km s^{-1}) and a prominent gradient is seen in the mean velocity field with a maximum difference of ≈ 360 km s^{-1} between spaxels in the north-east versus south-west corners of COS-87259 (Fig. 3).

(iii) Strong 158 μm dust continuum emission is also detected from COS-87259 with a surface brightness profile consistent with a compact (major axis $= 1.4 \pm 0.2$ kpc) core and a more extended (major axis $= 7.8 \pm 1.0$ kpc) region of emission (Fig. 2), similar to

that of the [C II] line. The combined flux density of these two dust continuum components is measured to be 2.71 ± 0.16 mJy and is almost equally divided among the two components (55 ± 4 per cent from the compact core).

(iv) COS-87259 exhibits the second most luminous and third broadest [C II] line known at $z > 6.5$ and the 158 μm dust continuum monochromatic luminosity of this system is also very similar to that of the IR-brightest $z \sim 7$ quasar host galaxies (Fig. 4). The ALMA data therefore indicate that COS-87259 is among the most extreme objects known in the reionization era in terms of its far-IR properties, suggesting it is likely one of the most massive galaxies at $z \sim 7$ with a very large star formation rate.

(v) The centroids of the [C II] and dust continuum emission are consistent within uncertainties, though we identify significant offsets between the ALMA centroids and the rest-UV as well as radio centroids. The ≈ 6 kpc projected separation between the 3 GHz detection peak and the [C II] + dust continuum centroids is to be expected if the radio emission is powered by an extended relativistic jet emerging from the AGN.

(vi) The MIPS, PACS, and SPIRE detections of COS-87259 indicate that this source harbours a heavily obscured AGN with a rest-frame 9.7 μm optical depth of $\tau_{9.7\,\mu m} = 2.3 \pm 0.1$, consistent with Compton-thick absorption. The very large bolometric AGN luminosity of $(5.1 \pm 0.5) \times 10^{13} \, L_\odot$ implies that COS-87259 is a highly obscured version of an $M_{1450} \approx -27.3$ quasar at $z \sim 7$ and is powered by a $\gtrsim 1.5 \times 10^9 \, M_\odot$ black hole (assuming an Eddington ratio of $\lesssim 1$). Comparably luminous quasars are an exceedingly rare population at $z \sim 7$ (~ 0.001 deg^{-2}; Wang et al. 2019), while COS-87259 was identified over a relatively small (1.5 deg^2) area. Wider area searches for very luminous ($L_{bol} \gtrsim 10^{13} \, L_\odot$) heavily obscured AGNs at $z > 6$ will be required to better assess how common this population is relative to quasars.

(vii) The 158 μm dust continuum emission suggests that COS-87259 is forming stars at a rate of $\approx 1300 \, M_\odot$ yr^{-1}, consistent with the estimate from the near-IR through millimetre SED fit ($\approx 1610 \, M_\odot$ yr^{-1}). Regardless of the exact value, it is clear from the strong ALMA detections that COS-87259 is undergoing vigorous obscured star formation activity comparable to $z \sim 7$ sub-mm galaxies and quasar hosts. The VIRCam and IRAC photometry of COS-87259 suggests that its rest-UV + optical emission is powered by star formation rather than by the AGN. Under this assumption, we estimate an extremely large stellar mass of $(1.7 \pm 0.7) \times 10^{11} \, M_\odot$ for COS-87259, though different assumptions on star formation history can yield significantly lower mass estimates given existing broad-band photometry (E22a; van Mierlo et al. 2022a; Whitler et al. 2023). None the less, all stellar mass estimates of COS-87259 are at least an order of magnitude lower than that expected from local scaling relations between the properties of supermassive black holes and their host galaxies.

Future wide-area data sets will provide a greatly improved understanding of the incidence of heavily obscured supermassive black hole growth and dust-enshrouded stellar mass build-up within the most massive reionization-era galaxies. Within the coming decade, surveys with *Roman* and *Euclid* are expected to cover hundreds to thousands of square degrees with optical + near-IR (0.9–2 μm) depths of $m_{5\sigma} \sim 26$–27 (Spergel et al. 2015; Euclid Collaboration 2022; van Mierlo et al. 2022b). These surveys will therefore enable the identification of extremely red ($\beta > -1$) yet UV-bright ($M_{UV} \lesssim -21.5$) $z \gtrsim 7$ galaxies like COS-87259 over a much wider area via the presence of very strong ($\gtrsim 3$ mag) Lyman-alpha breaks. Sensitive follow-up at mid/far-IR, radio, and X-ray wavelengths will provide

the opportunity to investigate both obscured star formation as well as heavily obscured AGN activity within these sources, delivering a much clearer picture of the typical characteristics of the most massive reionization-era galaxies. Such studies will complement searches of red yet relatively unobscured quasars (e.g. Kato et al. 2020; Fujimoto et al. 2022), radio-selected AGNs (e.g. Smith et al. 2016; Saxena et al. 2018; Broderick et al. 2022), and X-ray-selected AGNs (Nandra et al. 2013; Weisskopf et al. 2015) in the reionization epoch to build a more complete census of early supermassive black hole growth mechanisms.

DATA AVAILABILITY

The ALMA data that are the focus of this article are publicly available on the ALMA science archive (2021.1.01311.S). The remaining data on COS-87259 are detailed in E22a.
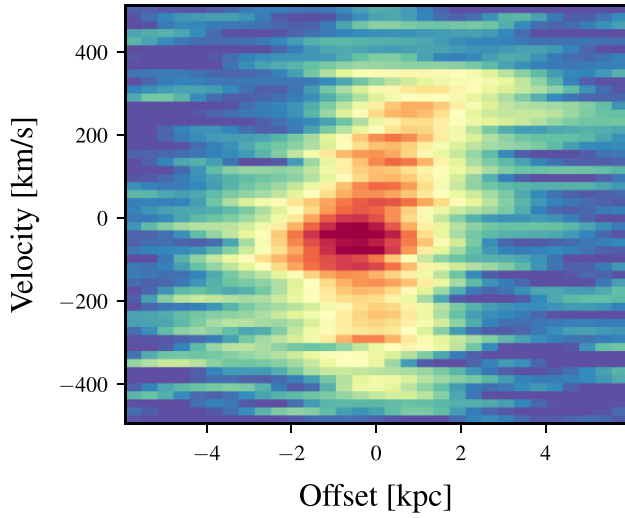
REFERENCES

Aihara H. et al., 2019, PASJ, 71, 114
Aihara H. et al., 2022, PASJ, 74, 247
Assef R. J. et al., 2015, ApJ, 804, 27
Astropy Collaboration, 2013, A&A, 558, A33
Auger M. W., Treu T., Bolton A. S., Gavazzi R., Koopmans L. V. E., Marshall P. J., Moustakas L. A., Burles S., 2010, ApJ, 724, 511
Bañados E., Decarli R., Walter F., Venemans B. P., Farina E. P., Fan X., 2015, ApJ, 805, L8
Bañados E. et al., 2018, Nature, 553, 473
Bañados E. et al., 2021, ApJ, 909, 80
Beelen A., Cox P., Benford D. J., Dowell C. D., Kovács A., Bertoldi F., Omont A., Carilli C. L., 2006, ApJ, 642, 694
Bouwens R. J. et al., 2011, ApJ, 737, 90
Bouwens R. J., Illingworth G. D., Oesch P. A., Caruana J., Holwerda B., Smit R., Wilkins S., 2015, ApJ, 811, 140
Bouwens R. J. et al., 2021, AJ, 162, 47
Bouwens R. J. et al., 2022, ApJ, 931, 160
Bowler R. A. A., Dunlop J. S., McLure R. J., McLeod D. J., 2017, MNRAS, 466, 3612
Bowler R. A. A., Jarvis M. J., Dunlop J. S., McLure R. J., McLeod D. J., Adams N. J., Milvang-Jensen B., McCracken H. J., 2020, MNRAS, 493, 2059
Bowler R. A. A., Cullen F., McLure R. J., Dunlop J. S., Avison A., 2022, MNRAS, 510, 5088
Broderick J. W. et al., 2022, Publ. Astron. Soc. Aust., 39, e061
Calzetti D., Armus L., Bohlin R. C., Kinney A. L., Koornneef J., Storchi-Bergmann T., 2000, ApJ, 533, 682
Carniani S. et al., 2018, MNRAS, 478, 1170
Circosta C. et al., 2019, A&A, 623, A172
Civano F. et al., 2016, ApJ, 819, 62
Conroy C., Gunn J. E., 2010, ApJ, 712, 833
Conroy C., Gunn J. E., White M., 2009, ApJ, 699, 486
Davies F. B., Hennawi J. F., Eilers A.-C., 2019, ApJ, 884, L19
De Barros S., Oesch P. A., Labbé I., Stefanon M., González V., Smit R., Bouwens R. J., Illingworth G. D., 2019, MNRAS, 489, 2355
De Rossi M. E., Rieke G. H., Shivaei I., Bromm V., Lyu J., 2018, ApJ, 869, 4
Decarli R. et al., 2017, Nature, 545, 457
Decarli R. et al., 2018, ApJ, 854, 97
Decarli R. et al., 2022, A&A, 662, A60
Eilers A.-C., Hennawi J. F., Davies F. B., 2018, ApJ, 867, 30
Eilers A.-C. et al., 2020, ApJ, 900, 37
Eilers A.-C., Hennawi J. F., Davies F. B., Simcoe R. A., 2021, ApJ, 917, 38
Eisenhardt P. R. M. et al., 2012, ApJ, 755, 173
Ellis R. S. et al., 2013, ApJ, 763, L7
Endsley R., Stark D. P., 2022, MNRAS, 511, 6042
Endsley R., Stark D. P., Chevallard J., Charlot S., 2021a, MNRAS, 500, 5229
Endsley R., Stark D. P., Charlot S., Chevallard J., Robertson B., Bouwens R. J., Stefanon M., 2021b, MNRAS, 502, 6044
Endsley R. et al., 2022a, MNRAS, 512, 4248
Endsley R. et al., 2022b, MNRAS, 517, 5642
Euclid Collaboration, 2022, A&A, 662, A112
Everett W. B. et al., 2020, ApJ, 900, 55
Fan L., Han Y., Nikutta R., Drouart G., Knudsen K. K., 2016, ApJ, 823, 107
Finkelstein S. L. et al., 2015, ApJ, 810, 71
Finkelstein S. L. et al., 2019, ApJ, 879, 36
Fudamoto Y. et al., 2021, Nature, 597, 489
Fujimoto S. et al., 2022, Nature, 604, 261
Furusawa H. et al., 2016, ApJ, 822, 46
Giavalisco M. et al., 2004, ApJ, 600, L93
Ginolfi M. et al., 2020, A&A, 633, A90
Grogin N. A. et al., 2011, ApJS, 197, 35
Harikane Y. et al., 2022, ApJS, 259, 20
Häring N., Rix H.-W., 2004, ApJ, 604, L89
Harris C. R. et al., 2020, Nature, 585, 357
Hashimoto T. et al., 2019, PASJ, 71, 71
Herrera-Camus R. et al., 2015, ApJ, 800, 1

Hopkins P. F. et al., 2004, AJ, 128, 1112
Hunter J. D., 2007, Comput. Sci. Eng., 9, 90
Illingworth G. D. et al., 2013, ApJS, 209, 6
Inami H. et al., 2022, MNRAS, 515, 3126
Inayoshi K., Visbal E., Haiman Z., 2020, ARA&A, 58, 27
Inoue A. K. et al., 2020, PASJ, 72, 101
Ishigaki M., Kawamata R., Ouchi M., Oguri M., Shimasaku K., Ono Y., 2018, ApJ, 854, 73
Izumi T. et al., 2021, ApJ, 908, 235
Jarvis M. J. et al., 2013, MNRAS, 428, 1281
Johnson B. D., Leja J., Conroy C., Speagle J. S., 2021, ApJS, 254, 22
Kato N. et al., 2020, PASJ, 72, 84
Koekemoer A. M. et al., 2011, ApJS, 197, 36
Kroupa P., 2001, MNRAS, 322, 231
Labbé I. et al., 2013, ApJ, 777, L19
Lawrence A. et al., 2007, MNRAS, 379, 1599
Lotz J. M. et al., 2017, ApJ, 837, 97
Lupi A., Volonteri M., Decarli R., Bovino S., Silk J., 2022, MNRAS, 510, 5760
Lyu J., Rieke G., 2022, Universe, 8, 304
Lyu J., Rieke G. H., Alberts S., 2016, ApJ, 816, 85
Lyu J., Rieke G. H., Shi Y., 2017, ApJ, 835, 257
Lyu J., Alberts S., Rieke G. H., Rujopakarn W., 2022, ApJ, 941, 191
Maiolino R. et al., 2012, MNRAS, 425, L66
Marconi A., Risaliti G., Gilli R., Hunt L. K., Maiolino R., Salvati M., 2004, MNRAS, 351, 169
Marrone D. P. et al., 2018, Nature, 553, 51
Mason C. A., Trenti M., Treu T., 2015, ApJ, 813, 21
Matsuoka Y. et al., 2018, ApJS, 237, 5
Matsuoka Y. et al., 2019, ApJ, 883, 183
Matsuoka Y. et al., 2022, ApJS, 259, 18
Matthee J. et al., 2019, ApJ, 881, 124
Mazzucchelli C. et al., 2017, ApJ, 849, 91
McCracken H. J. et al., 2012, A&A, 544, A156
McLure R. J. et al., 2013, MNRAS, 432, 2696
McMullin J. P., Waters B., Schiebel D., Young W., Golap K., 2007, in Shaw R. A., Hill F., Bell D. J., eds, ASP Conf. Ser. Vol. 376, Astronomical Data Analysis Software and Systems XVI. Astron. Soc. Pac., San Francisco, p. 127
Morey K. A., Eilers A.-C., Davies F. B., Hennawi J. F., Simcoe R. A., 2021, ApJ, 921, 88
Mortlock D. J. et al., 2011, Nature, 474, 616
Murphy E. J. et al., 2011, ApJ, 737, 67
Nandra K. et al., 2013, preprint (arXiv:1306.2307)
Neeleman M. et al., 2019, ApJ, 882, 10
Neeleman M. et al., 2021, ApJ, 911, 141
Ni Y., Di Matteo T., Gilli R., Croft R. A. C., Feng Y., Norman C., 2020, MNRAS, 495, 2135
Novak M. et al., 2020, ApJ, 904, 131
Oesch P. A., Bouwens R. J., Illingworth G. D., Labbé I., Stefanon M., 2018, ApJ, 855, 105
Oke J. B., Gunn J. E., 1983, ApJ, 266, 713
Ono Y. et al., 2012, ApJ, 744, 83
Pei Y. C., 1992, ApJ, 395, 130
Pensabene A., Carniani S., Perna M., Cresci G., Decarli R., Maiolino R., Marconi A., 2020, A&A, 637, A84
Pensabene A. et al., 2021, A&A, 652, A66
Pentericci L. et al., 2016, ApJ, 829, L11
Price-Whelan A. M. et al., 2018, AJ, 156, 123
Reed S. L. et al., 2017, MNRAS, 468, 4702
Reed S. L. et al., 2019, MNRAS, 487, 1874
Richards G. T. et al., 2003, AJ, 126, 1131
Robertson B. E., 2022, ARA&A, 60, 121
Runnoe J. C., Brotherton M. S., Shang Z., 2012, MNRAS, 422, 478
Saxena A. et al., 2018, MNRAS, 480, 2733
Schouws S. et al., 2022a, preprint (arXiv:2202.04080)
Schouws S. et al., 2022b, ApJ, 928, 31

Selsing J., Fynbo J. P. U., Christensen L., Krogager J. K., 2016, A&A, 585, A87
Shen X., Hopkins P. F., Faucher-Giguère C.-A., Alexander D. M., Richards G. T., Ross N. P., Hickox R. C., 2020, MNRAS, 495, 3252
Shi Y. et al., 2006, ApJ, 653, 127
Shivaei I. et al., 2020, ApJ, 899, 117
Simpson J. M. et al., 2019, ApJ, 880, 43
Smit R. et al., 2014, ApJ, 784, 58
Smit R. et al., 2015, ApJ, 801, 122
Smit R. et al., 2018, Nature, 553, 178
Smith D. J. B. et al., 2016, in Reylé C., Richard J., Cambrésy L., Deleuil M., Pécontal E., Tresse L., Vauglin I., eds, SF2A-2016: Proc. Annu. Meeting French Soc. Astron. Astrophys. Centre de Recherche Astrophysique de Lyon, p. 271
Smolčić V. et al., 2017, A&A, 602, A1
Song M. et al., 2016, ApJ, 825, 5
Speagle J. S., 2020, MNRAS, 493, 3132
Spergel D. et al., 2015, preprint (arXiv:1503.03757)
Spilker J. S. et al., 2022, ApJ, 929, L3
Stark D. P., Schenker M. A., Ellis R., Robertson B., McLure R., Dunlop J., 2013, ApJ, 763, 129
Stefanon M. et al., 2019, ApJ, 883, 99
Stefanon M., Bouwens R. J., Labbé I., Illingworth G. D., Gonzalez V., Oesch P. A., 2021, ApJ, 922, 29
Strandet M. L. et al., 2017, ApJ, 842, L15
Topping M. W. et al., 2022, MNRAS, 516, 975
Trakhtenbrot B. et al., 2015, Science, 349, 168
Trebitsch M., Volonteri M., Dubois Y., 2019, MNRAS, 487, 819
Trenti M. et al., 2011, ApJ, 727, L39
Tsai C.-W. et al., 2015, ApJ, 805, 90
Valentino F. et al., 2022, ApJ, 929, L9
van Mierlo S. E., Caputi K. I., Kokorev V., 2022a, preprint (arXiv:2212.04511)
van Mierlo S. E. et al., 2022b, A&A, 666, A200
Venemans B. P. et al., 2012, ApJ, 751, L25
Venemans B. P. et al., 2013, ApJ, 779, 24
Venemans B. P. et al., 2015, ApJ, 801, L11
Venemans B. P., Walter F., Zschaechner L., Decarli R., De Rosa G., Findlay J. R., McMahon R. G., Sutherland W. J., 2016, ApJ, 816, 37
Venemans B. P. et al., 2017a, ApJ, 845, 154
Venemans B. P. et al., 2017b, ApJ, 851, L8
Venemans B. P., Neeleman M., Walter F., Novak M., Decarli R., Hennawi J. F., Rix H.-W., 2019, ApJ, 874, L30
Venemans B. P. et al., 2020, ApJ, 904, 130
Virtanen P. et al., 2020, Nat. Methods, 17, 261
Vito F. et al., 2018, MNRAS, 473, 2378
Wang F. et al., 2017, ApJ, 839, 27
Wang F. et al., 2018, ApJ, 869, L9
Wang F. et al., 2019, ApJ, 884, 30
Wang F. et al., 2021, ApJ, 907, L1
Weaver J. R. et al., 2022, ApJS, 258, 11
Weisskopf M. C., Gaskin J., Tananbaum H., Vikhlinin A., 2015, in Hudec R., Pina L., eds, Proc. SPIE Conf. Ser. Vol. 9510, EUV and X-ray Optics: Synergy between Laboratory and Space IV. SPIE, Bellingham, p. E2
Whitler L., Stark D. P., Endsley R., Leja J., Charlot S., Chevallard J., 2023, MNRAS, 519, 5859
Willott C. J., Bergeron J., Omont A., 2017, ApJ, 850, 108
Yang J. et al., 2019a, AJ, 157, 236
Yang J. et al., 2019b, ApJ, 880, 153
Yang G. et al., 2020a, MNRAS, 491, 740
Yang J. et al., 2020b, ApJ, 897, L14
Yang J. et al., 2021, ApJ, 923, 262
Yue M. et al., 2021, ApJ, 917, 99

APPENDIX A: PV DIAGRAM

We show the position–velocity diagram of [C II]158 μm emission from COS-87259 in Fig. A1.

Figure A1. The position–velocity diagram of [C II]158 μm emission from COS-87259 extracted along the major axis. There is no clear evidence of multiple distinct components separated in velocity space.

This paper has been typeset from a TEX/LATEX file prepared by the author.